THE ASTROPHYSICAL JOURNAL, 638:L117–L120, 2006 February 20

RHESSI AND *SOHO* CDS OBSERVATIONS OF EXPLOSIVE CHROMOSPHERIC EVAPORATION

RYAN O. MILLIGAN,[1,2] PETER T. GALLAGHER,[2,3,4] MIHALIS MATHIOUDAKIS,[1] D. SHAUN BLOOMFIELD,[1]
FRANCIS P. KEENAN,[1] AND RICHARD A. SCHWARTZ[2,5]

Received 2005 September 9; accepted 2005 December 19; published 2006 January 27

ABSTRACT

Simultaneous observations of explosive chromospheric evaporation are presented using data from the *Reuven Ramaty High-Energy Solar Spectroscopic Imager* (*RHESSI*) and the Coronal Diagnostic Spectrometer (CDS) on board the *Solar and Heliospheric Observatory*. For the first time, cospatial imaging and spectroscopy have been used to observe explosive evaporation within a hard X-ray emitting region. *RHESSI* X-ray images and spectra were used to determine the flux of nonthermal electrons accelerated during the impulsive phase of an M2.2 flare. When we assumed a thick-target model, the injected electron spectrum was found to have a spectral index of ~7.3, a low-energy cutoff of ~20 keV, and a resulting flux of $\geq 4 \times 10^{10}$ ergs cm^{-2} s^{-1}. The dynamic response of the atmosphere was determined using CDS spectra; we found a mean upflow velocity of 230 $\pm$ 38 km s^{-1} in Fe XIX (592.23 Å) and associated downflows of 36 $\pm$ 16 and 43 $\pm$ 22 km s^{-1} at chromospheric and transition region temperatures, respectively, relative to an averaged quiet-Sun spectra. The errors represent a 1 σ dispersion. The properties of the accelerated electron spectrum and the corresponding evaporative velocities were found to be consistent with the predictions of theory.

Subject headings: Sun: atmospheric motions — Sun: flares — Sun: UV radiation — Sun: X-rays, gamma rays

Online material: color figure

1. INTRODUCTION

Current solar flare models (Antiochos & Sturrock 1978; Fisher et al. 1984, 1985a, 1985b, 1985c; Mariska et al. 1989) predict two types of chromospheric evaporation processes. "Gentle" evaporation occurs when the chromosphere is heated either directly by nonthermal electrons or indirectly by thermal conduction. The chromospheric plasma subsequently loses energy via a combination of radiation and low-velocity hydrodynamic expansion. "Explosive" evaporation takes place when the chromosphere is unable to radiate energy at a sufficient rate and consequently expands at high velocities into the overlying flare loops. The overpressure of evaporated material also drives low-velocity downward motions into the underlying chromosphere, in a process known as chromospheric condensation.

From a theoretical perspective, Fisher et al. (1985a) investigated the relationship between the flux of nonthermal electrons (F) and the velocity response of the atmosphere for the two classes of evaporation. For gentle evaporation, nonthermal electron fluxes of $\leq 10^{10}$ ergs cm^{-2} s^{-1} were found to produce upflow velocities of tens of kilometers per second. In contrast, explosive evaporation was found to be associated with higher nonthermal electron fluxes ($F \geq 3 \times 10^{10}$ ergs cm^{-2} s^{-1}), which drive both upflows of hot material at velocities of several hundred kilometers per second *and* downflows of cooler material at tens of kilometers per second.

Observationally, previous studies have identified blueshifted soft X-ray and EUV lines indicative of chromospheric evaporation. Using the Bent Crystal Spectrometer on board the *Solar Maximum Mission*, Antonucci & Dennis (1983) and Zarro & Lemen (1988) reported upflow velocities of 400 and 350 km s^{-1}, respectively, in Ca XIX lines (3.1–3.2 Å). More recently, Czaykowska et al. (1999), Teriaca et al. (2003), and Del Zanna et al. (2006) observed velocities of 140–200 km s^{-1} in Fe XIX (592.23 Å), using the Coronal Diagnostic Spectrometer (CDS; Harrison et al. 1995) on board the *Solar and Heliospheric Observatory* (*SOHO*). Simultaneous upflows and downflows during a hard X-ray (HXR) burst indicative of explosive evaporation have been observed using CDS and the *Yohkoh* Hard X-Ray Telescope by Brosius & Phillips (2004). While these studies provided a measurement of the dynamic response of the flaring chromosphere, they were unable to provide a measurement of the flux of electrons responsible for driving such motions nor the spatial relationship between the two.

In this Letter, simultaneous *Reuven Ramaty High-Energy Solar Spectroscopic Imager* (*RHESSI*; Lin et al. 2002) and CDS observations are combined for the first time to investigate the relationship between the nonthermal electron flux and the response of the solar atmosphere. In § 2, the analysis techniques employed are described, while the results are presented in § 3. Our conclusions are then given in § 4.

2. OBSERVATIONS AND DATA ANALYSIS

This study focuses on a *Geostationary Operational Environmental Satellite* M2.2 flare, which began at 12:44 UT on 2003 June 10. The event was selected from a sample of approximately 50 flares jointly observed by *RHESSI* and CDS. The limited field of view, cadence, and operating schedule of CDS, coupled with *RHESSI* nighttime and South Atlantic Anomaly passes, make simultaneous observations by the two instruments quite rare.

2.1. *The Coronal Diagnostic Spectrometer*

The CDS observations reported here were obtained with the FLARE_AR observing sequence. FLARE_AR contains five ≤ 4 Å wide spectral windows centered on He I (584.33 Å; $\log T = 4.5$), O V (629.73 Å; $\log T = 5.4$), Mg X (624.94 Å; $\log T = 6.1$), Fe XVI (360.76 Å; $\log T = 6.4$), and Fe XIX (592.23 Å; $\log T = 6.9$). Each raster consists of 45 slit positions,

[1] Department of Physics and Astronomy, Queen's University Belfast, University Road, Belfast, BT7 1NN, Ireland; r.milligan@qub.ac.uk.
[2] Laboratory for Astronomy and Solar Physics, NASA Goddard Space Flight Center, Greenbelt, MD 20771.
[3] School of Physics, Trinity College Dublin, Dublin 2, Ireland.
[4] L-3 Communications GSI.
[5] Science Systems and Applications, Inc., 10210 Greenbelt Road, Lanham, MD 20706.

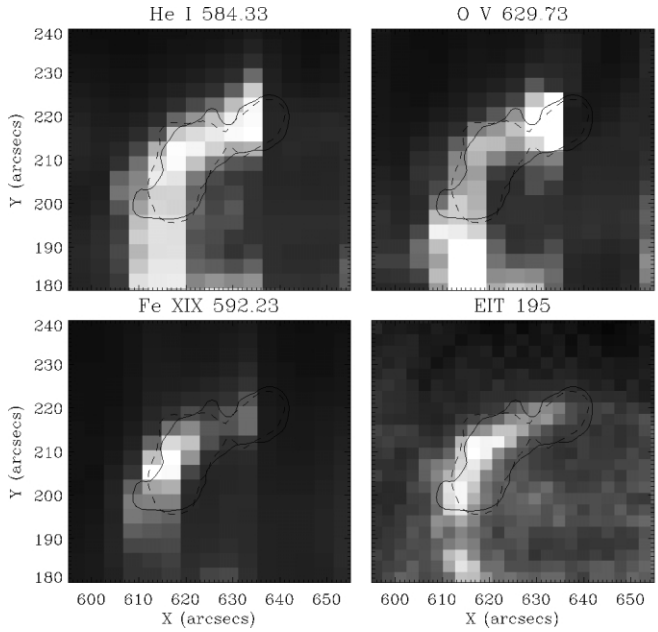

FIG. 1.—CDS images in the He I, O V, and Fe XIX emission lines observed during the impulsive phase of the flare, with the corresponding EIT 195 Å image. *RHESSI* 12–25 keV (*dashed lines*) and 25–60 keV (*solid lines*) contours are overlaid, each drawn at 10% of the peak intensity. [*See the electronic edition of the Journal for a color version of this figure*.]

each ~15 s long, resulting in an effective cadence of ~11 minutes. The slit itself is $4'' \times 180''$, yielding a $\sim 180'' \times 180''$ field of view. A zoomed-in region of the He I, O V, and Fe XIX rasters from the impulsive phase of the flare is given in Figure 1. Also shown is the EUV Imaging Telescope (EIT; Delaboudinière et al. 1995) 195 Å passband image obtained at 12:48 UT. A series of subsequent EIT images makes it clear that the He I and O V brightenings come from a flare ribbon rather than two distinct footpoints, as Figure 1 may suggest.

The spectrum from each CDS pixel was fitted with a broadened Gaussian profile (Thompson 1999), for each of the five spectral windows. Velocity maps were created by measuring Doppler shifts relative to quiet-Sun spectra, which were assumed to be emitted by stationary plasma. Preliminary fits to the Fe XIX line during the impulsive phase of the flare revealed an asymmetric broadening beyond the instrumental resolution of CDS. The strongest blue asymmetries were found within the flare ribbon during the impulsive phase. Outside this area, and after the impulsive phase, the Fe XIX line was observed to have a width comparable to the instrumental width. Figure 2 shows a sample of spectra taken from the spectral window centered on the Fe XIX (592.23 Å) emission line. Figure 2*a* shows a spectrum from a quiet-Sun area in which no Fe XIX emission was visible. Instead, a weak emission line was observed at 592.6 Å, which Del Zanna & Mason (2005) have identified as Fe XII. Figure 2*b* shows a stationary Fe XIX emission line extracted from a bright region, but after the impulsive phase at ~12:50 UT when no significant flows are expected. An emission line with a strong blue asymmetry is shown in Figure 2*c*. This was extracted from the flare ribbon during the impulsive phase. The best fit to this line was consistent with stationary and blueshifted components, both with widths comparable to the instrumental resolution. As Fe XIX is not observed in quiet-Sun spectra, and following from Teriaca et al. (2003), the Doppler velocity was measured as the shift between these two components. A heliographic correction was also applied, due to the longitude of the observations and assuming purely radial flows.

2.2. *The Reuven Ramaty High-Energy Spectroscopic Imager*

RHESSI is an imaging spectrometer capable of observing X- and γ-ray emission over a wide range of energies (~3 keV–17 MeV). During this event, the thin attenuators on *RHESSI* were in place, thus limiting the energy range to $\gtrsim$6 keV. Flare emission was not observed above ~60 keV. The flare light curves are shown in the top panel of Figure 3. Both the *RHESSI* images and spectra were obtained over a 64 s period from 12:47:34 to 12:48:38 UT to coincide with the time range over which CDS observed blue asymmetries in the Fe XIX line. This time interval lies within the impulsive 25–60 keV HXR burst and is indicated by two vertical dotted lines in the top panel of Figure 3. *RHESSI* images in two energy bands (12–25 and 25–60 keV) were reconstructed using the *Pixon* algorithm (Hurford et al. 2002). Contours at 10% of the peak intensity in each band are overlaid on each EUV image in Figure 1.

The *RHESSI* spectrum was fitted assuming an isothermal distribution at low energies and thick-target emission at higher energies (Fig. 3, *bottom panel*). A thick-target model was chosen over a thin-target model, as it is believed that the density of the flare loop is insufficient to thermalize the electrons as they propagate to the chromosphere. The thick-target model is used in the vast majority of cases (e.g., Holman 2003; Veronig et al. 2005). Furthermore, in this flare the HXR source is clearly

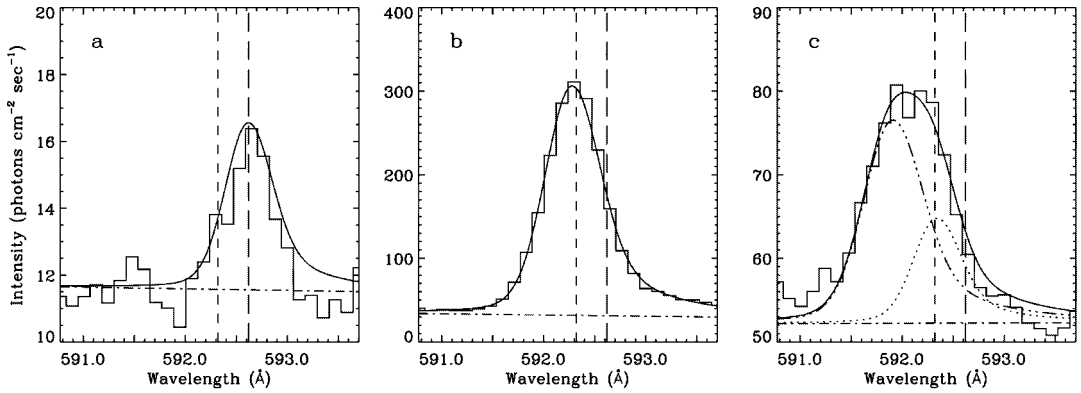

FIG. 2.—Sample of spectra from the spectral window centered on Fe XIX (592.23 Å). The vertical short-dashed line shows the rest wavelength of the Fe XIX line at 592.32 Å, while the long-dashed line shows the rest wavelength of the Fe XII line at 592.62 Å. Panel *a* was obtained from a quiet-Sun region, panel *b* shows a stationary Fe XIX line from a postimpulsive phase flare kernel, while panel *c* shows an Fe XIX line from the flare ribbon during the impulsive phase. The dotted line indicates the stationary component, while the triple-dot–dashed line indicates the blueshifted component.

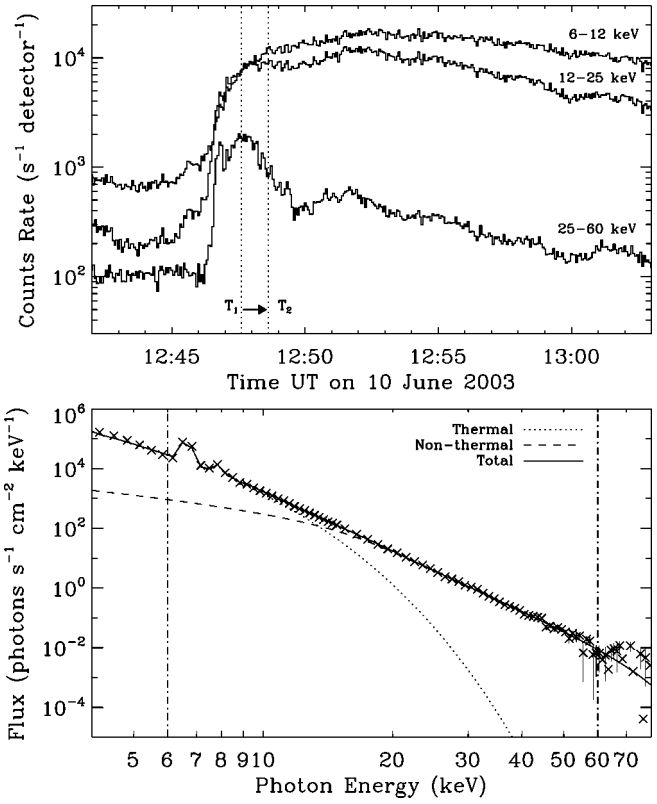

FIG. 3.—*Top panel*: *RHESSI* light curves from the 6–12, 12–25, and 25–60 keV bands. The dotted vertical lines indicate the time interval over which images and spectra were obtained to correspond to time when significant upflows were observed using CDS. *Bottom panel*: Portion of the *RHESSI* spectrum integrated over the time range given above. The energy range 6–60 keV (*vertical dot-dashed lines*) was fitted with an isothermal component (*dotted curve*) and a thick-target bremsstrahlung component (*dashed curve*).

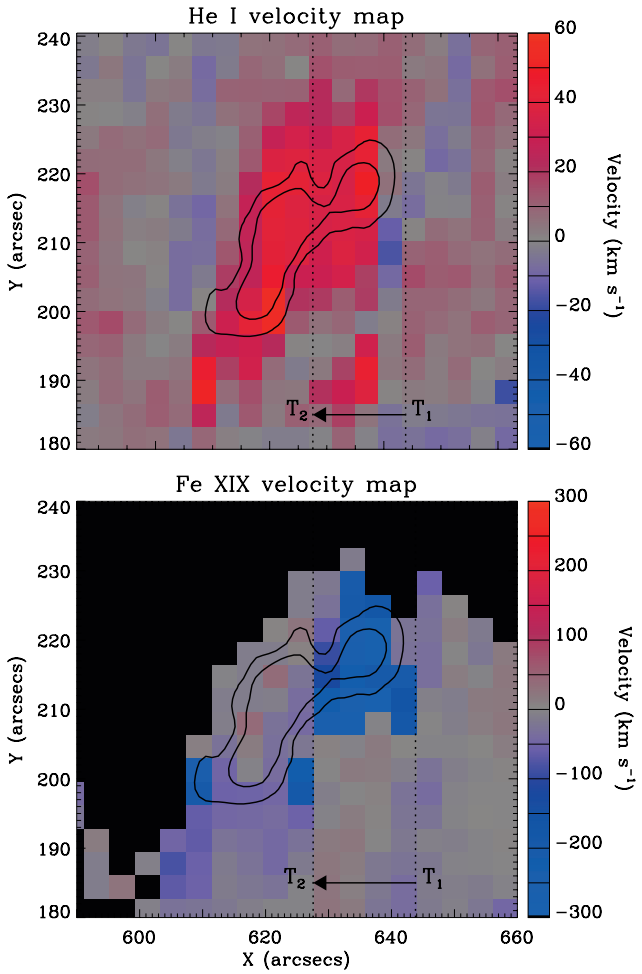

FIG. 4.—Velocity maps in He I and Fe XIX. Downflows are indicated by red pixels, while upflows are indicated by blue pixels. The vertical dashed lines correspond to the times indicated by the vertical dashed lines in Fig. 3, and the arrow denotes the direction in which the CDS slit moves. Black regions in the Fe XIX map represent pixels where no significant Fe XIX emission was observed. *RHESSI* 25–60 keV contours at 10% and 40% of the peak intensity are overlaid.

aligned with the He I ribbon as seen by CDS, which implies that the accelerated electrons are losing their energy in the dense chromosphere rather than in the coronal loops. The total power of nonthermal electrons above the low-energy cutoff (ϵ_c) was calculated from $P(\epsilon \geq \epsilon_c) = \int_{\epsilon_c}^{\infty} f_e(\epsilon) d\epsilon$ ergs s^{-1}, where $f_e(\epsilon) \sim \epsilon^{-\delta}$ electrons keV^{-1} s^{-1} is the thick-target electron injection spectrum and δ is the associated spectral index (Brown 1971). Because of the steepness of the *RHESSI* spectrum at high energies, the nonthermal flux is quite sensitive to the value of the low-energy cutoff. In order to put a constraint on this value, the temperature of the thermal component was obtained by another independent method, i.e., the equivalent width of the Fe line complex at 6.7 keV (Phillips 2004). The value of the equivalent width of this line, which is quite sensitive to the temperature, was used to estimate the temperature of the thermal component. Having fixed this value, the entire *RHESSI* spectrum was fitted using a least-squares fit.

3. RESULTS

The thick-target model fitted to the *RHESSI* spectrum in Figure 3 was consistent with an electron distribution having $\epsilon_c \sim 20$ keV and $\delta \sim 7.3$. The break energy of 20 keV is consistent with earlier works (e.g., Holman 2003; Sui et al. 2005). The total power in nonthermal electrons was therefore 1×10^{29} ergs s^{-1}. Exploring the possible range of values for the break energy for this flare would yield an electron power value of 4×10^{29} ergs s^{-1} for $\epsilon_c = 15.0$ keV, while $\epsilon_c = 25.0$ keV would give a power value of 6×10^{28} ergs s^{-1}. However, either of these break energies would give a worse χ^2-value than obtained from the original fit. By comparison, the total thermal power for the same time interval was found to be 1.2×10^{28} ergs s^{-1}.

Using the reconstructed 25–60 keV image, we calculate the upper limit to the source size to be 2.3×10^{18} cm^2. This was found by summing over all pixels with counts greater than 10% of the peak value. This threshold was chosen to eliminate sources outside of the main HXR-emitting region, which were assumed to be unreal; the source area was not found to be highly sensitive to this value. For example, a threshold of 5% yielded an area of 3.2×10^{18} cm^2 and 15% yielded 2×10^{18} cm^2. This area was also confirmed using the Fourier modulation profiles from each of *RHESSI*'s nine detectors, which are sensitive to spatial scales from 2.″2 to 183″. Assuming a filling factor of unity, we calculated the resulting nonthermal electron flux to be $\geq 4 \times 10^{10}$ ergs cm^{-2} s^{-1}.

Figure 4 shows velocity maps in the He I and Fe XIX lines. The He I map shows consistent downflows of 20–50 km s^{-1} until the slit leaves the flaring region at ~12:50 UT. A velocity map in O V showed a similar trend. However, the Fe XIX map shows strong upflow velocities of 190–280 km s^{-1} during the

HXR peak, indicated by "T_1" and "T_2" on Figures 3 and 4. No significant upflows were evident once the HXRs begin to diminish from time T_2 onward.

By identifying each pixel in the Fe XIX map that required a two-component fit to the line profile, between times T_1 and T_2, the velocity was measured for the corresponding pixel in each of the five CDS rasters. Figure 5 shows the mean velocity as a function of temperature for each line using the methods described in § 2. The error bars represent a 1 σ dispersion. At chromospheric and transition region temperatures, plasma velocities show redshifts of 36 ± 16 and 43 ± 22 km s^{-1}, respectively, while the blueshift observed in the 8 MK Fe XIX line corresponds to a velocity of 230 ± 38 km s^{-1}. No significant flows were observed in the Mg X and Fe XVI lines. The combination of high-velocity upflows and low-velocity downflows, together with a nonthermal electron flux of $\geq 4 \times 10^{10}$ ergs cm^{-2} s^{-1}, provides clear evidence for explosive chromospheric evaporation.

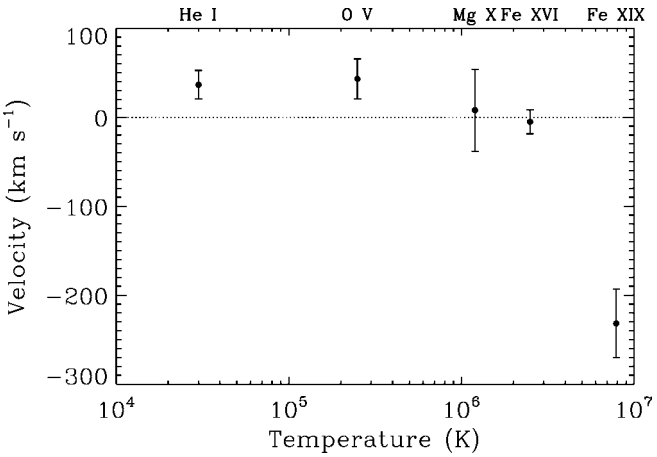

FIG. 5.—Plasma velocity as a function of temperature for the five lines observed using CDS. Positive velocities indicate downflows, while negative values indicate upflows.

4. DISCUSSION AND CONCLUSIONS

For the first time, cospatial and cotemporal HXR and EUV observations of chromospheric evaporation are presented using *RHESSI* and *SOHO* CDS. High upflow velocities (~230 km s^{-1}) were clearly observed in high-temperature Fe XIX emission during the impulsive phase of an M2.2 flare, while much lower downflow velocities (~40 km s^{-1}) were observed in the cooler He I and O V lines. The value of the nonthermal electron flux ($\geq 4 \times 10^{10}$ ergs cm^{-2} s^{-1}) and the resulting velocity response are indicative of an explosive evaporation process occurring during this flare, as laid out in Fisher et al. (1985a) and Mariska et al. (1989).

The combination of HXR and EUV observations presented in this Letter have enabled us to obtain a greater understanding of the characteristics of chromospheric evaporation, a fundamental process in solar flares. We have presented the first detection of explosive mass motions within HXR footpoints and determined the flux of nonthermal electrons responsible for driving such flows.

This work has been supported by a Department of Employment and Learning studentship and a Cooperative Award in Science and Technology. F. P. K. is grateful to A. W. E. Aldermaston for the award of a William Penny Fellowship. We would like to thank Brian Dennis, Joe Gurman, and Dominic Zarro at NASA Goddard Space Flight Center for their stimulating discussion and continued support. We would also like to thank the anonymous referee for their comments and suggestions, which have greatly improved this Letter. *SOHO* is a project of international collaboration between the European Space Agency and NASA.

REFERENCES

Antiochos, S. K., & Sturrock, P. A. 1978, ApJ, 220, 1137
Antonucci, E., & Dennis, B. R. 1983, Sol. Phys., 86, 67
Brosius, J. W., & Phillips, K. J. H. 2004, ApJ, 613, 580
Brown, J. C. 1971, Sol. Phys., 18, 489
Czaykowska, A., De Pontieu, B., Alexander, D., & Rank, G. 1999, ApJ, 521, L75
Delaboudinière, J. -P., et al. 1995, Sol. Phys., 162, 291
Del Zanna, G., Berlicki, A., Schmieder, B., & Mason, H. E. 2006, Sol. Phys., in press
Del Zanna, G., & Mason, H. E. 2005, A&A, 433, 731
Fisher, G. H., Canfield, R. C., & McClymont, A. N. 1984, ApJ, 281, L79
———. 1985a, ApJ, 289, 414
———. 1985b, ApJ, 289, 425
———. 1985c, ApJ, 289, 434
Harrison, R. A., et al. 1995, Sol. Phys., 162, 233
Holman, G. D. 2003, ApJ, 586, 606
Hurford, G. J., et al. 2002, Sol. Phys., 210, 61
Lin, R. P., et al. 2002, Sol. Phys., 210, 3
Mariska, J. T., Emslie, A. G., & Li, P. 1989, ApJ, 341, 1067
Phillips, K. J. H. 2004, ApJ, 605, 921
Sui, L., Holman, G. D., & Dennis, B. R. 2005, ApJ, 626, 1102
Teriaca, L., Falchi, A., Cauzzi, G., Falciani, R., Smaldone, L. A., & Andretta, V. 2003, ApJ, 588, 596
Thompson, W. T. 1999, Post-Recovery Broadened Line Profiles (CDS Software Note 53; Chilton: Rutherford Appleton Lab.)
Veronig, A. M., Brown, J. C., Dennis, B. R., Schwartz, R. A., Sui, L., & Tolbert, A. K. 2005, ApJ, 621, 482
Zarro, D. M., & Lemen, J. R. 1988, ApJ, 329, 456